

www.acsami.org Research Article

The Role of SnO₂ Processing on Ionic Distribution in Double-Cation-Double Halide Perovskites

Holland Hysmith, So Yeon Park, Jonghee Yang, Anton V. Ievlev, Yongtao Liu, Kai Zhu, Bobby G. Sumpter, Joseph Berry, Mahshid Ahmadi,* and Olga S. Ovchinnikova*



Cite This: ACS Appl. Mater. Interfaces 2023, 15, 36856–36865



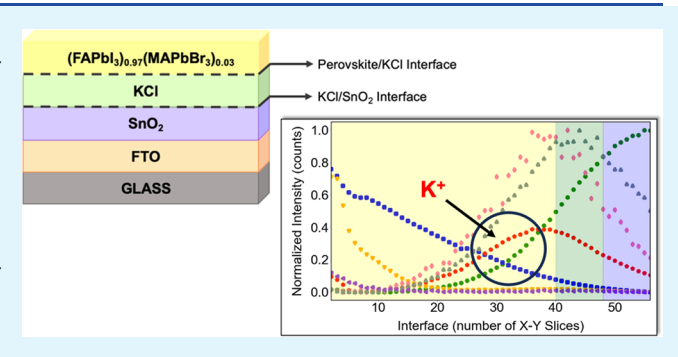
ACCESS I

Metrics & More

Article Recommendations

Supporting Information

ABSTRACT: Moving toward a future of efficient, accessible, and less carbon-reliant energy devices has been at the forefront of energy research innovations for the past 30 years. Metal-halide perovskite (MHP) thin films have gained significant attention due to their flexibility of device applications and tunable capabilities for improving power conversion efficiency. Serving as a gateway to optimize device performance, consideration must be given to chemical synthesis processing techniques. Therefore, how does common substrate processing techniques influence the behavior of MHP phenomena such as ion migration and strain? Here, we demonstrate how a hybrid approach of chemical bath deposition (CBD) and nanoparticle SnO₂ substrate processing significantly



improves the performance of (FAPbI₃)_{0.97}(MAPbBr₃)_{0.03} by reducing micro-strain in the SnO₂ lattice, allowing distribution of K⁺ from K-Cl treatment of substrates to passivate defects formed at the interface and produce higher current in light and dark environments. X-ray diffraction reveals differences in lattice strain behavior with respect to SnO2 substrate processing methods. Through use of conductive atomic force microscopy (c-AFM), conductivity is measured spatially with MHP morphology, showing higher generation of current in both light and dark conditions for films with hybrid processing. Additionally, time-of-flight secondary ionization mass spectrometry (ToF-SIMS) observed the distribution of K⁺ at the perovskite/SnO₂ interface, indicating K⁺ passivation of defects to improve the power conversion efficiency (PCE) and device stability. We show how understanding the role of ion distribution at the SnO2 and perovskite interface can help reduce the creating of defects and promote a more efficient MHP device.

KEYWORDS: metal-halide perovskite, tin oxide, time-of-flight secondary ionization mass spectrometry, conductive atomic force microscopy

INTRODUCTION

Metal-halide perovskite (MHP) photovoltaics (PV) is leading the way toward scalable, flexible, and affordable energy devices with a reported efficiency of a single junction cell close to 26%.1 However, a major bottleneck to large-scale MHP implementation is long-term stability. Degradation due to ion migration under operational conditions is one mechanistic pathway of concern. It is known that the MHPs' structural stability can change under an ambient environment² and illumination³ (i.e., degradation), as well as thermal stress⁴ (i.e., strain) leading to an unstable behavior. Defect formation in MHPs can happen in two ways: during film formation or during subsequent device operation. More specifically, the intrinsic MHP defects occur through Schottky and Frenkel defects during synthesis and crystallization, the former reducing carrier lifetime and the latter creating unintentional doping. Extrinsic defects also associated with film processing are grain boundaries, interfaces, and pinholes, which can contribute to ionic mobility in MHPs.7 Device degradation typically originates at the interface between perovskite and

substrate as well as other interfacial layers. Processing can impact the interfacial structure through physical and chemical changes.8 Exploring the ways in which formation dynamics of the MHP active layer is impacted by the substrate, and to what extent defect formation and resulting device performance are impacted, is key to moving these MHP devices to the market. Therefore, understanding the role of processing on PV device performance, including the substrate layer (either electron or hole transport layers), can offer an opportunity for improving the outcome of performance as defined by operational efficiency and reliability.

As mentioned apart from MHP synthesis procedures, the substrate composition and surface chemistry produced by a

Received: March 10, 2023 Accepted: July 5, 2023 Published: July 20, 2023





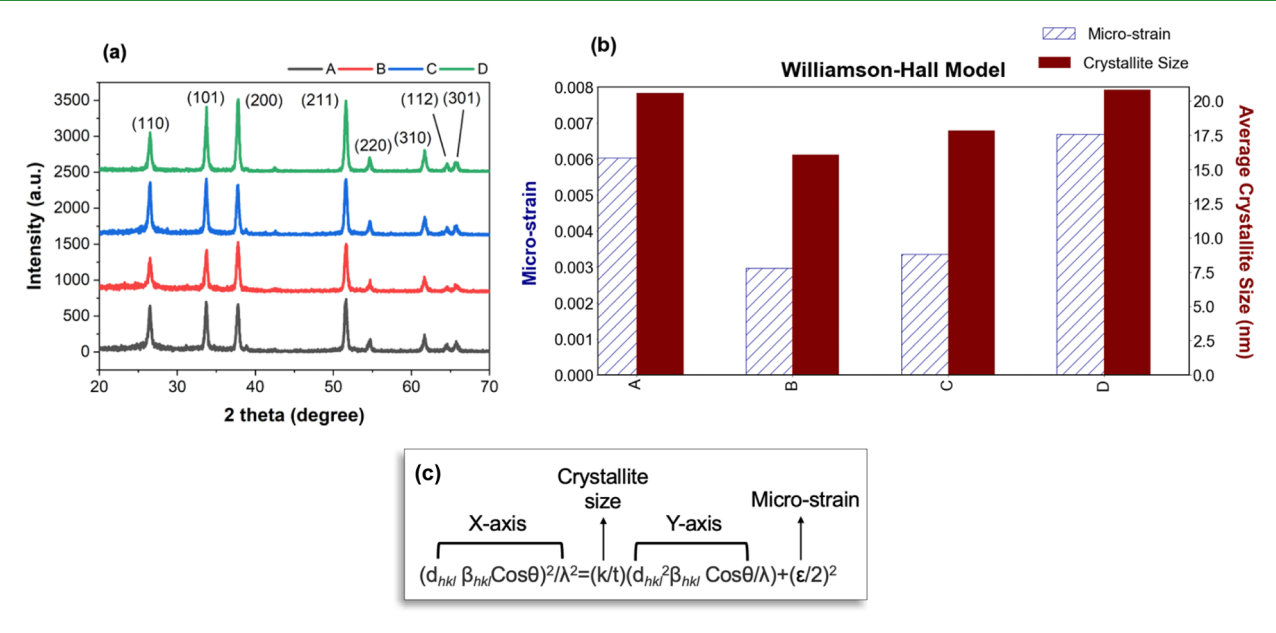


Figure 1. (a) X-ray diffraction patterns of A–D SnO₂ substrates. (b) Williamson–Hall size-strain plot method of bare SnO₂ substrates of A–D showing micro-strain (striped) and average crystallite size (solid). (c) Williamson–Hall size-strain calculation method of SnO₂ substrates, showcasing the best fit for small crystalline sizes (\sim 3–5 nm).

particular processing route can directly affect the crystalline structure of MHPs along with associated defects. 9-12 Many metal oxide substrate layers have been investigated (i.e., TiO₂, NiO_x)^{13,14} to understand what drives optimal power conversion efficiency (PCE) in MHP-based PV devices. For instance, TiO2 has been explored widely as a good electron transport layer (ETL) candidate in MHPs due to its high transport ability and lower conduction band compared to the perovskite active layer. 15 However, it must overcome oxygen vacancies acting as trap sites and conduction band offset influencing flow of photogenerated electrons from the perovskite layer to TiO₂. ¹⁶ On the other hand, NiO_x is frequently used as a hole transport layer (HTL) in MHPs due to its wide bandgap, amenable to a low-temperature process. However, physical defects such as pinholes and island morphology are re-occurring problems in NiOx and are yet to be resolved.¹⁴ Methods of the synthesis approach and substrate composition both play a part in achieving high performance.1

The substrate/MHP interaction can also influence the MHP defect structure and in turn impact the mobility of cation and halide ions during operation. For example, lead (Pb⁺) and methylammonium (MA⁺) migration has been demonstrated at the TiO₂ and MHP perovskite interface impacting charge extraction and therefore contributing to hysteresis effects. The influence of migration in mesoporous TiO₂ and compact TiO₂ is still not understood, showcasing the complexity of how substrate structure affects the ion migration. Additionally, TiO₂ can promote halide migration through hole accumulation and trapping iodide in MHPs, which creates unstable lattice sites for segregation to occur. Similar to TiO₂, SnO₂ can create compact layers that demonstrate better durability, optical properties, and thermal stability.

Indeed, of the current class of metal oxide substrates, SnO₂ has been considered a standout to its counterparts due to its wide bandgap and low-temperature processing. ¹⁹ Its significant contribution to MHP stability is the strain behavior between the perovskite and substrate interface. Strain relationships of

the perovskite/substrate interface may also have a direct effect on cation and halide distribution. Changes in local composition are then likely avenues to change local strain and migration as well, but direct demonstrations of this remain elusive. Integration of treatments or additives to the SnO₂/ MHP interface can change the development of grains and grain boundary structures to improve efficiency.²⁰ When prepared with nanoparticles, SnO₂ has a highly crystalline form that aids in eliminating defect traps and minimize hysteresis.²¹ Using chemical bath deposition (CBD) as the deposition process, SnO₂ can develop fewer surface defects at the expense of long deposition times to reduce the opportunity for aggregation.² Consequently, hybridizing the approach of CBD and nanoparticle SnO₂ deposition on MHPs could provide a route to developing a stable and high-performing MHP device architecture. This has motivated us to explore the effect of SnO₂ substrate processing and strain on ion distribution at the substrate/MHP interface.

In this work, we investigated ion distribution as influenced by substrate processing and how the substrate layer can provide insight on (FAPbI₃)_{0.97}(MAPbBr₃)_{0.03} stability and PCE optimization. Simple-structured systems, like MAPbI₃, have been previously explored to help with our general insights into the strain effect and ion migration behaviors associated with the SnO₂/perovskite interface.²³ Complex FA⁺-based MHPs with only trace amounts of MAPbBr3 deposited on SnO₂ substrates have produced devices exceeding 24% PCE.²⁴ We demonstrate a novel multimodal chemical imaging approach underpinned by machine learning (ML) data analysis to unravel chemistry changes throughout the MHP layer when formed on SnO₂ substrates prepared with CBD, nanoparticles (3-5 nm), and two hybridization approaches. Using conductive atomic force microscopy (c-AFM), we confirm thin films, which produce the highest levels of current and lead to a higher PCE with respect to different substrate processing techniques. Additionally, time-of-flight secondary ionization mass spectrometry (ToF-SIMS) explores the ionic distribution through the sample stack with depth profiling. Such profiles are

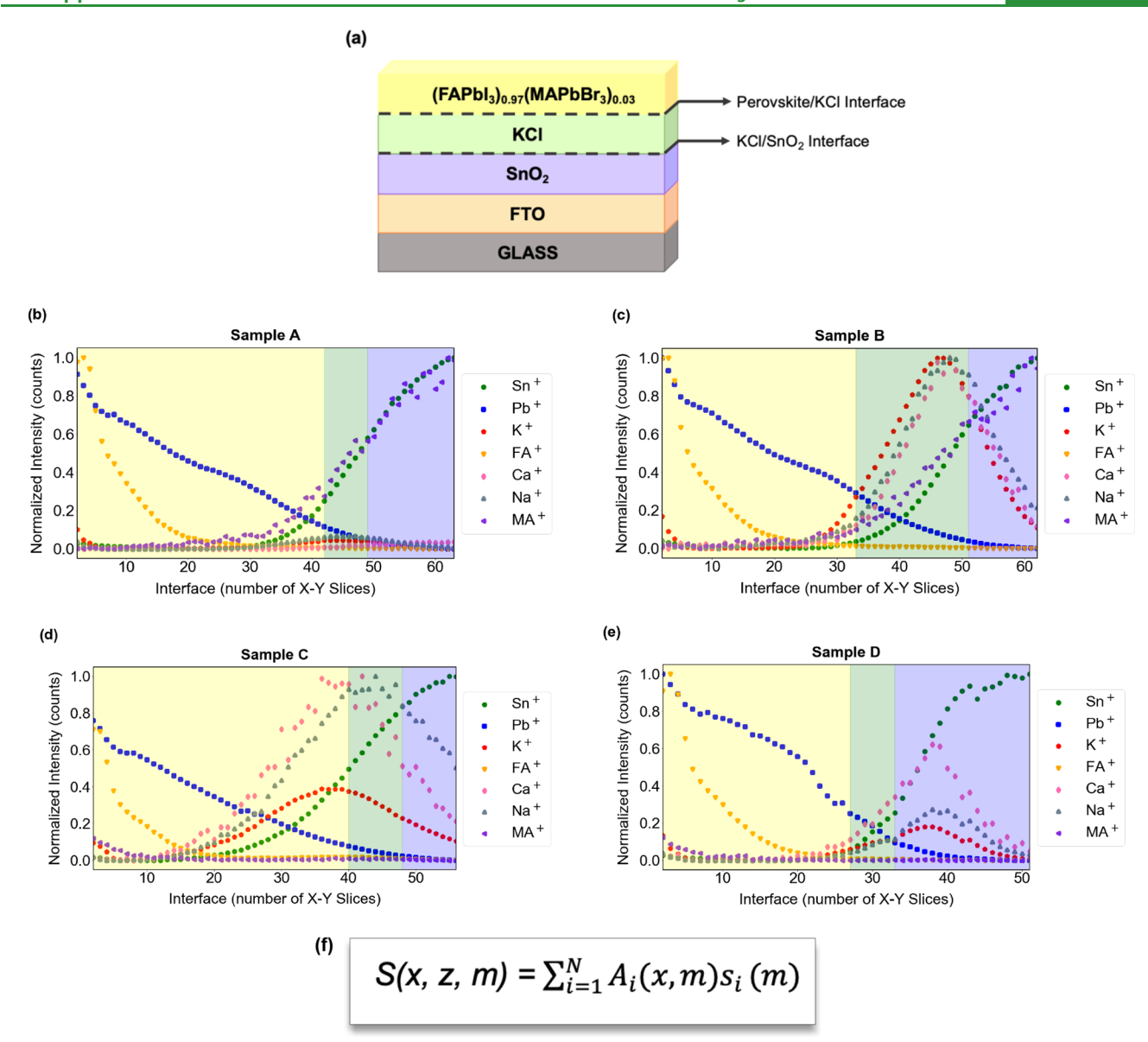


Figure 2. (a) Schematic of the MHP sample stack with dashed lines indicating the location of interfaces: perovskite/KCl and KCl/SnO₂. Depth profiling of (b-e) all samples highlighting the ionic migration with respect to each interface in positive ion mode. Each color shading represents a sample layer: perovskite (yellow), KCl (green), and SnO₂ (purple). Corresponding NMF mass spectral components are in Figure S12. (f) Nonnegative matrix factorization (NMF) equation.

extracted with non-negative matrix factorization (NMF) to segment profiles with each of the following interfaces: perovskite/KCl and KCl/SnO₂. Through this discovery, we show how the processing impacts the strain behavior of the SnO₂ layer and subsequent effects on ion migration and current performance in MHPs. Our results show that these findings will allow an opportunity for optimization of substrates to reduce defects that inhibit MHP performance.

RESULTS AND DISCUSSION

A series of (FAPbI₃)_{0.97}(MAPbBr₃)_{0.03} thin films were spin coated on the SnO₂ substrate, which were prepared using four different methods: CBD, nanoparticles, and two hybrid approaches of CBD and nanoparticles reacted for different thicknesses. The fabricated perovskite films showed nominal grain sizes and roughness in comparison to bare SnO2, exhibited in Figures S1-S4, featuring the grain size distribution

and mean square roughness for all samples. Samples were notated with respect to their processing technique: sample A prepared with CBD, sample D with nanoparticles, and samples B and C with hybrid processing. The difference between hybrid samples B and C is that the thickness of the SnO₂ layer is 70-80 nm for B and ~130 nm for C due to film reaction with nanoparticles being 4 h for B and 12 h for C. For additional reference, the SnO₂ thickness in samples A and D is 30-60 nm. To help reduce defect formation at the perovskite/ substrate interface, all SnO2 substrates were pre-treated with K-Cl through K⁺ passivation. ²⁵ From J-V curves seen in Figure S5 and representative values in Table S1, PCE values are calculated in the following order from highest to lowest: B, C, D, and A samples (or devices). Additionally, in Figure S6, samples A and D have I-V behavior similar to each other, possibly due to similar makeup in their morphology contrasting what is seen in B and C.

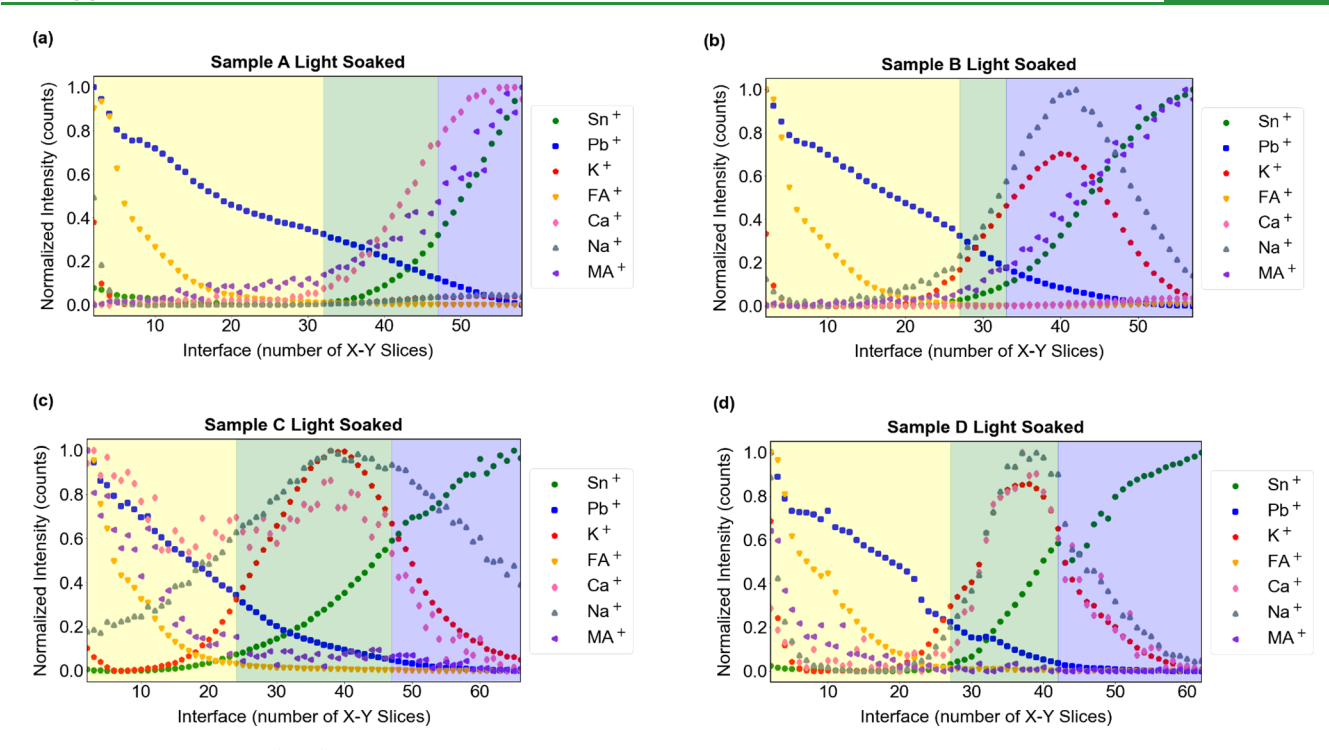


Figure 3. Depth profiling of (a–d) all light-soaked samples highlighting the ionic migration with respect to each interface in positive ion mode. Each color shading represents a sample layer: perovskite (yellow), KCl (green), and SnO₂ (blue). Corresponding NMF mass spectral components are in Figure S13.

To understand the influence of substrate processing on defect formation in the SnO2 substrate, we studied the strain behavior on bare SnO2 substrates prepared via different processing techniques. Characterization of X-ray diffraction (XRD) patterns was conducted on the SnO₂ substrate for A-D to correlate the relationship of micro-strain with substrate processing. Featured in Figure 1a, each substrate peak profile has the same peak location and broadening behavior among all processing techniques. The Williamson-Hall (W-H) plot analysis was conducted to measure the micro-strain in the substrates with respective crystallite sizes, as summarized in Figure 1b. The W-H calculation is optimal for smaller crystallites sizes (<~10 nm) and is used for this study because the average SnO₂ nanoparticle size ranges 3-5 nm. Assuming deformation in all lattice directions, this technique measures the lattice distance among the (hkl) planes, and by plotting this relationship, featured in Figure 1c and Figure S7, the crystallite size is represented from the slope and micro-strain from the yintercept.²⁶

The results of the XRD pattern and W–H analysis identified the hybrid B substrate as having the lowest micro-strain and average crystallite size of 2.98×10^{-3} and 16.06 nm, respectively.²⁷ Hybrid sample C, with greater thickness compared to B, has the second lowest values with a microstrain of 3.35×10^{-3} and crystallite size of 17.86 nm. This shows that smaller crystallite sizes in the hybrid SnO_2 layer reduce lattice spacing of the *hkl* planes, preventing large areas for defect formation to occur. Such results can also point to fewer pinholes and better uniformity for the hybrid B and C samples. Mis-matched alignment from the influence of external stress (by micro-strain of the SnO_2 substrate) can lead to residual tensile strain in MHP, which weakens the lattice integrity.²⁸ This indicates that devices with higher efficiency like B have a lower strain to allow for distribution of cations

(i.e., such as K⁺) at the perovskite/SnO₂ interface to occur. This will be explored later where we discuss the ToF-SIMS observations. Additionally, to differentiate the strain observed at the perovskite/SnO2 interface, XRD with the added perovskite layer of A-D is featured in Figure S8 and corresponding W-H analysis featured in Figure S9. Radial distribution function (RDF) models are used to further understand how lattice spacing between ions changes with respect to different compositions and environmental conditions like tensile strain.²⁹ RDF models featured in Figures S10 and S11 show decreased distances for cations-anions in the hybrid MAPbBr₃-FAPbI₃ case, especially between the metals and anions. The decreased distance leads both to a favorable change in the electronic structure and to the pathways for ion mobility.³⁰ Observing the chemistry changes across the MHP interfaces will show how the behavior of ion distribution changes with respect to each substrate processing

To understand the evolution of chemistry across the interfaces in MHP samples, a ToF-SIMS depth profiling analysis was undertaken.³¹ ToF-SIMS offers a unique capability of providing extensive chemical distribution information with respect to depth and surface profile imaging.³² Using a 1 keV oxygen dual source ion column (DSC) to sputter, all thin films were monitored for spectral changes to indicate the perovskite/SnO₂ interface. This interface was defined at the intersection where the intensity of Sn⁺ in SnO₂ surpassed the intensity of Pb⁺ in (FAPbI₃)_{0.97}(MAPbBr₃)_{0.03}. Intermediate regions between the perovskite/SnO2 interface (i.e., perovskite/KCl and KCl/SnO₂) were also observed due to the migration of K+ into the perovskite layer from the KCl treatment of SnO₂. To separate the spatial complexity of the depth profiles in a multicomponent dataset, an NMF was applied using four components: (1) perovskite surface, (2)

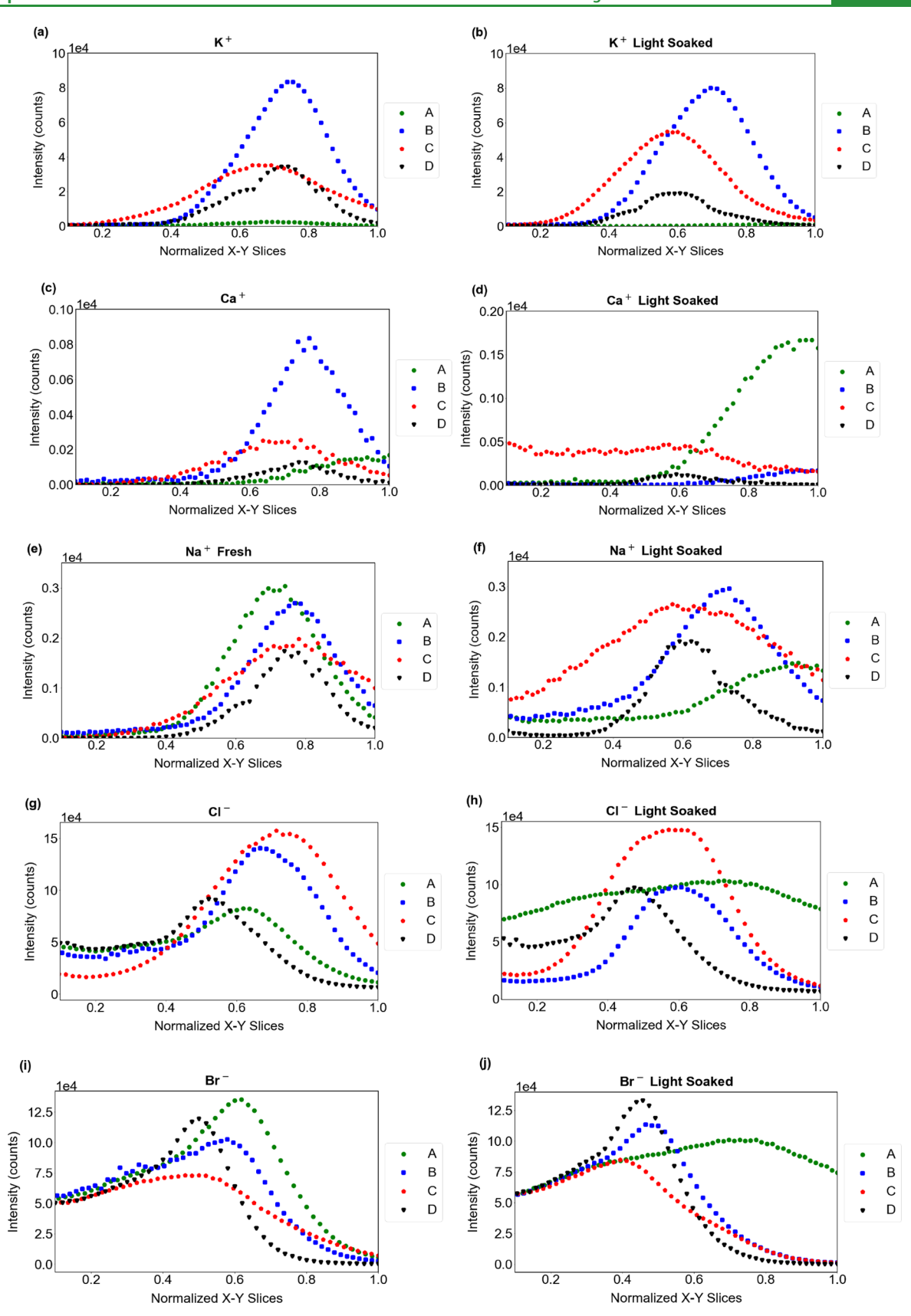


Figure 4. (a—h) Depth profiling of all samples before and after light soaking showing the ionic distribution of K⁺, Ca⁺, Cl⁻, and Br⁻. All plots were normalized to similarly compare differences in ionic distribution.

perovskite layer, (3) perovskite/KCl interface, and (4) KCl/SnO₂ interface demonstrated in Figures S12–S17. Shown in

Figure 2f, NMF was calculated as a function of "x", the fraction of individual ions, "m", individual ion mass, and "z", the cross

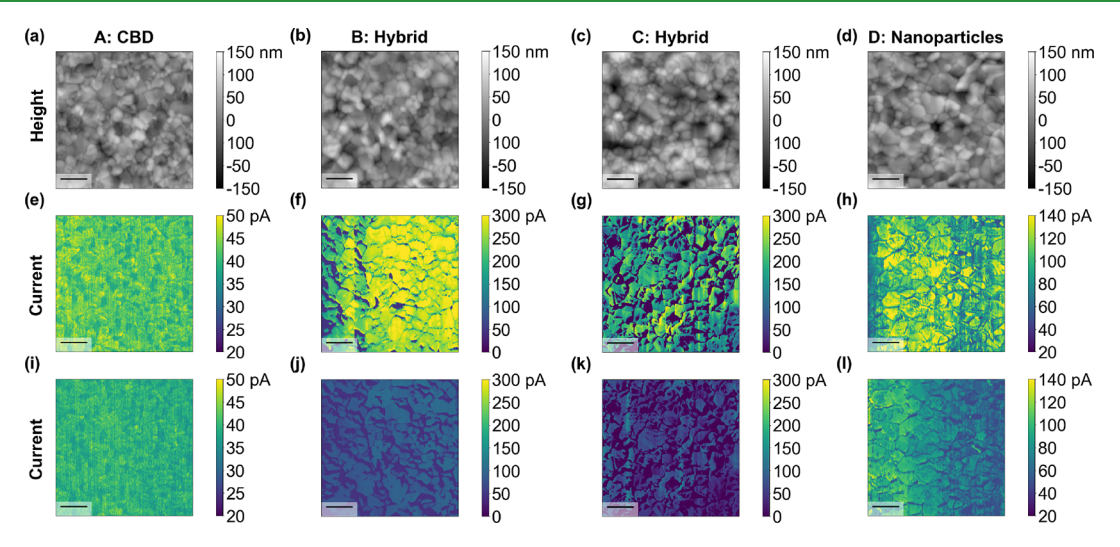


Figure 5. (a-d) Height images of A-D samples and corresponding current images under (e-h) illumination and (i-l) dark conditions. Scale bar: $2 \mu m$. The duration of the scans took approximately 12 min, switching optical light in between scans.

section of the device surface through the depth profile. ^{33,34} One-dimensional loading maps as a function of depth were extracted and corresponded to NMF endmembers. These endmembers represent ions indicated in the mass spectra at each interface.

Depth profiling was conducted in positive and negative ion modes to track spectral counts located at each interface. Positive ions with high counts such as Pb+, tin (Sn+), and potassium (K⁺) were detected through the film depth profiles, seen in Figure 2. For MHP samples with hybrid SnO₂ substrate processing (B and C), the presence of K⁺ ions was significant at the perovskite/SnO2 interface, in sample B surpassing the intensity of the Pb⁺ and Sn⁺ intersection itself demonstrated in Figure 2c, and with smaller intensity in sample C in Figure 2d. This phenomenon of K+ surpassing the intersection was not present in samples with exclusive CBD or nanoparticle substrate processing (A and D samples), shown in Figure 2b and e, respectively. Originating from the K-Cl pre-treatment of the SnO₂ substrates, ToF-SIMS was used to confirm and observe the distribution of K⁺ at the perovskite/SnO₂ interface. Greater distribution of K+ ions in hybrid samples can be a result of higher K+ diffusion and passivating defects at the interface and therefore reducing micro-strain behavior in this sample. Hybrid sample B has greater K+ distribution in comparison to hybrid sample C, likely due to 80 nm being thinner, allowing greater diffusion in the SnO₂ layer. Additionally, Pb⁺ and Sn⁺ counts and distribution are similar in both samples B and C at the perovskite/SnO₂ interface.

To explore the stability and ion distribution under sunlight, we have studied the ToF-SIMS analysis of the same samples by exposing them to 120 suns for light soaking, seen in Figure 3. The hybrid B and C samples have a similar behavior prior to light soaking for K^+ distribution at the interface of the perovskite/SnO₂ substrate seen in Figure 3b and c, respectively. The intensity of K^+ ions in sample B surpasses that of Pb⁺ and Sn⁺ at the perovskite/SnO₂ interface (i.e., intersection point of both signals). Similar counts of Pb⁺, Sn⁺, and K^+ are shown after light soaking as well, demonstrating robust stability and the ions at interfaces after sun exposure. In Figure 3d, the distribution of K^+ is seen in sample D after light soaking. Although showing significantly smaller K^+ intensity at the interface, sample D is prepared with nanoparticles and

therefore may allow for easier K^+ distribution since an insignificant K^+ distribution is seen in sample A before and after light soaking. Negative ion distributions before and after light soaking are featured in Figure S18. Unlike positive ion trends, negative ion distribution did not show any substantial features unique to SnO_2 processing methods.

Other ions such as sodium (Na⁺), calcium (Ca⁺), formamidinium (FA+), and MA+ are seen in the spectral analysis as well in Figures 2 and 3. Yet, the intensity of counts for all positive and negative ions differs among samples; therefore, individual ions were plotted separately for comparison in Figure 4 and Figures S19 and S20. Migration of Na+ and Ca+ ions is primarily shown in samples B through D, likely from the soda lime glass (SLG) and could also be capable of passivating defects in the perovskite/SnO2 layer and resisting illumination degradation. 35,36 This trend is also seen across all samples after light soaking, featured in Figure 3. However, the roles of Na⁺ and Ca⁺ cannot be explicitly determined due to their extremely low counts. Therefore, it is believed that the primary mechanism behind defect passivation at the perovskite/SnO2 interface is K+ ions from the K-Cl treatment of SnO₂. Across all samples, Figure S19e-h shows greater distribution of FA⁺ near the perovskite surface and greater MA⁺ distribution near the SnO₂ layer before and after light soaking. The disparity between these ions in the perovskite layer could influence the K+ distribution in the perovskite. MA+ have a smaller ionic radius compared to FA+ and therefore could allow more sites for K⁺ at the interface. Both Pb⁺ and Sn⁺ maintained consistency before and after light soaking through constant decreasing and increasing ionic distribution, respectively, with each interface. Featured in Figure 4g-h for negative ion mode, Cl⁻ distribution is seen at the perovskite/SnO₂ interface as expected when coupled with the K⁺ distribution prior to light soaking, yet it does not follow the trend as closely as K⁺ after light soaking. Therefore, this confirms that K+ is driving the defect passivation at the interface. Additionally, Br distribution is noted with no particular trend with respect to sample preparation either before or after light soaking. Featured in Figure S20, distributions of halide ions such as I-, SnO-, and I2- were observed before and after light soaking. Similar counts can be seen for all negative ions mentioned, further indicating that

only positive ion distribution had a significant change from the hybrid processing technique in comparison to the other samples. Consistent with previous reports, these results also indicate that passivation ions can reduce defects without the need of changing the composition of the ETL layer, opening more possibilities to use cost-efficient and sustainable substrates.

Next, investigation into the conductivity behavior can help uncover if the role of K⁺ passivating defects produces higher current in hybrid samples. To explore the conductivity of the MHP thin films on the SnO₂ substrates, we performed c-AFM measurements featured in Figure 5. This measurement allows us to compare the morphology and spatial distribution of photocurrent and dark current in the MHP thin films deposited on SnO₂ substrates prepared with different processing techniques.³⁷ To understand the spatial trends of photocurrent and dark current with respect to grains and grain boundaries, we conduct c-AFM measurements under illumination and dark conditions. For illumination conditions, a white LED light source was positioned to illuminate the sample from the top. The topography of each location featured in Figure 5a-d was scanned simultaneously with current, to compare the film morphology with the current response. The morphology of the films was uniform throughout the series, not differing significantly with respect to their processing techniques. In samples prior to light soaking, a higher photocurrent output (pA) is shown when illuminated, as shown in Figure 5e-h versus when in darkness seen in Figure 5i-l. All devices displayed a higher current response within grains versus at the grain boundaries. Lower current is detected at defect sites like grain boundaries due to it potentially functioning as a recombination site,³⁸ although the role of grain boundaries is still highly debated and out of the scope of this study. 39,40 Crystallographic grains and their orientation can cause inter-heterogeneity of current response within grains, similar to what is demonstrated across these devices.⁴¹ Also, inhomogeneous current distribution across samples can contribute to the distribution of K+-passivating defect sites at the perovskite/ SnO_2 interface.⁴²

While the systematic study exploring the structure-property relationships associated with the strain-controlled MHP films utilizing spatially resolved electrical and chemical characterization techniques is required, the global impact of K+ distribution in the MHP films is evidenced by the c-AFM analysis. 38,40,43,44 With the micro-strain control, we observed that hybrid B and C samples generate higher conductivity in light and dark conditions compared to samples A and D. These results are in agreement with Figure S5 and Table S1 featuring the calculated PCE from I-V curves. Sample B, which represents the most efficient solar cell in the series, produces photocurrent upward of 300 pA in light on and 120 pA in dark conditions. Additionally, light-soaked samples are observed in Figure S21. Although subject to light-induced degradation from sun exposure, B and C samples still demonstrate higher levels of current after light soaking in comparison to A and D samples. The light-soaked C sample increased the most in production of photocurrent at 500 pA under light and 90 pA in the dark. Such results also indicate less susceptibility to breakdown under illumination at the surface/perovskite interface in hybrid devices. Additionally, hybrid samples B and C have lower micro-strain, allowing greater distribution of K⁺ to passivate defects acting as recombination sites as shown

in ToF-SIMS analysis, therefore increasing current production 45

CONCLUSIONS

Using a hybrid method of CBD and nanoparticles for SnO₂ film deposition, a recorded PCE of 22% was achieved by (FAPbI₃)_{0.97}(MAPbBr₃)_{0.03} solar cells. This hybrid approach showed better MHP film performance and stability in comparison to using CBD or nanoparticle deposition of SnO₂ exclusively. XRD revealed hybrid sample B with the highest PCE to have the smallest crystallite size of 16.06 nm and a micro-strain value of 2.98×10^{-3} . Smaller crystallite sizes and lower micro-strain indicate smaller lattice spacing among the hkl planes, correlating to less defect formation in the SnO₂ substrate. Smaller micro-strain behavior in the SnO2 lattice indicated opportunity for greater distribution of K⁺ to occur for passivating defects at the perovskite/SnO₂ interface. K⁺ migration surpassed the perovskite/SnO2 interface in hybrid sample B. We did not observe significant change in distribution of ions in hybrid samples after light soaking exposure, indicating a stable mechanism. Higher conductivity is recorded in hybrid samples for both light and dark conditions, due to less defect formation in the SnO₂ substrate and at the perovskite/SnO₂ interface. Therefore, hybridizing CBD and nanoparticles on K-Cl-treated SnO₂ substrates with optimum thickness provides a viable pathway for improving the efficiency and stability of MHPs.

MATERIALS AND METHODS

Preparation of SnO₂ Films. The same chemicals for the precursor were used for all types of SnO₂ film. For preparation of the precursor for CBD, 1.25 g of urea (Sigma-Aldrich, CS reagent, 99%), 0.275 g of SnCl₂ 2H₂O (Sigma-Aldrich, ACS Reagent, 98%), 1.25 mL of HCl (Sigma-Aldrich, 37 wt %), and 0.025 mL of thioglycolic acid (Sigma-Aldrich, 98%) were added in 100 mL of DI water and mixed for 1 h.²⁴ Note that the precursor should be a clear solution. The cleaned fluorine-doped tin oxide (FTO) substrates were placed vertically in the precursor solution with the help of a holder and then reacted in a convention oven at 70 °C for 4 h (sample A). The SnO₂ nanoparticle solution was prepared by the sol-gel method using the reported method.⁴⁶ 1.25 g of urea and 0.275 g of SnCl₂ 2H₂O (Sigma-Aldrich, ACS Reagent, 98%) and 0.125 mL of HCl (Sigma-Aldrich, 37 wt %) were mixed in 10 mL of DI water and aged for 60 h at room temperature until the solution became clear yellowish. The synthesized SnO₂ nanoparticle solution was stored in a refrigerator to avoid aggregating particles easily. To prepare the SnO_2 nanoparticle film (sample D), the solution was spin-coated at 3000 rpm for 30 s onto UV-Ozone-treated FTO glass substrates. For preparation of a dense and thick SnO2 layer, 5 wt % of SnO2 nanoparticle solution was added in the precursor solution and stirred for 30 min at room temperature. Two different hybrid SnO2 films were reacted for 4 h (sample B) and 12 h (sample C) at 70 °C, respectively. Finally, the as-prepared SnO2/FTO samples were annealed at 150 °C for 2 h.

Preparation of the Perovskite Film and Device Fabrication. The perovskite $((\text{FAPbI}_3)_{0.97}(\text{MAPbBr}_3)_{0.03})$ film was deposited by one-step spin coating. To prepare the perovskite precursor solution, 1.55 M PbI₂, 1.55 M FAI, and 0.048 M MAPbBr₃ were dissolved in a mixed solvent (DMF/DMSO = 8:1) with 40 mol % MACl additive. Before deposition of perovskite, the 10 mM KCl solution was spin-coated (5000 rpm, 30 s) onto the UV-Ozone-treated SnO₂ film. Then, to fabricate the perovskite/SnO₂ film, the perovskite precursor solution was spin-coated on the SnO₂ film at 5000 rpm for 20 s and 1 mL of diethyl ether was gently dropped 10 s after spinning. The asspun perovskite film was annealed at 150 °C for 15 min in an ambient environment. The light-soaked samples were prepared using a sulfur

plasma lamp with an intensity of \sim 1.0 sun for 120 h. In addition, to finish the devices, spiro-OMeTAD solution was spin coated on the perovskite film at 4000 rpm for 30 s and a 100 nm gold electrode was deposited by thermal evaporation under a high vacuum pressure, as reported in our previous work. The photocurrent density—voltage (J-V) measurements were carried out under AM 1.5 G illumination (100 mW/cm², Oriel Sol3A Class AAA Solar Simulator) using a Keithley 2400 source meter. Both backward-scan and forward-scan curves were measured with a bias step of 10 mV.

XRD. The XRD and grazing incident XRD (GIXRD) of the $\rm SnO_2$ film were characterized using a Rigaku D Max 2200 diffractometer with Cu K α radiation and a scanning angle in the 2 theta range of 20–70°.

c-AFM. Measurements for c-AFM were taken on an Asylum Research MFP-3D Infinity AFM at the Center for Nanophase Material Sciences (CNMS) in Oak Ridge National Laboratory (ORNL). Samples were attached onto a glass slide with carbon tape and grounded with silver paint to a copper wire. Wiring was attached via alligator clips to the Infinity stage and ARC2 controller output. An ORCA conductive AFM probe holder was used to produce c-AFM images. A sample voltage range of 0.5–2.5 V was applied with a 1 V setpoint. The scan rate was set at 0.5 Hz for a series of 256 points and line images. Scanning duration took approximately 12 min, switching optical light in between scans.

ToF-SIMS. ToF-SIMS measurements were conducted on an AFM/FIB-ToF-SIMS instrument produced by ION-TOF at the CNMS. Samples were mounted onto a top-mount holder and grounded to the stage with silver paint. Depth profiling was conducted using a 30 kV bismuth LMIG and 1 keV oxygen DSC with a 100-micron field of view and 300-micron sputtering area. Mass spectra, depth profiles, and fast images were calibrated with SurfaceLab 7 software.

NMF. To identify the interfaces in the thin films for tracking ionic migration, an NMF analysis was conducted through Python's Scikitlearn package. ⁴⁸ The simsdata package developed by ORNL was used to extract and plot the overall mass spectra. The spectra transformed into 1D plots with separation into four components. The depth profiling maps were normalized from a time scale into data points. Each interface was identified by cross-referencing the intersection of the 1D components to the depth profiles.

Ab Initio Calculations. The Vienna Ab initio Simulation Package (VASP version 5.4.4)⁴⁹ using the projector-augmented wave (PAW) method⁵⁰ was used to study the effects of interfaces and strain. The electron-ion interactions were described using standard PAW potentials, with valence electron configurations of 5d¹⁰6s²6p² for Pb, 4s²4p⁵ for Br, 2s²2p² for C, 2s²2p³ for N, 1s¹ for H, 2s²2p⁴ for O, and 4d¹⁰5s²5p²for Sn. To account for van der Waals interactions, the vdW-DF method implemented by Dion et al. and modified by Klimeš et al. was employed. 51 The kinetic energy cutoff for plane waves was set to 400 eV, and the "normal" precision setting was adopted. GGA exchange-correlation potential with the Perdew-Burke-Ernzerhof (PBE) functional was used with a convergence criterion for the electronic self-consistent loop set to 10^{-4} eV. A supercell model of the low-energy stoichiometric (110) surface containing five Pb layers was constructed using the experimental X-ray structure of CH₃NH₃PbI₃ in a room-temperature tetragonal phase⁵² with I replaced with Br. DFT was used to optimize each model system, CH₃NH₃PbBr₃ (MAPbBr₃), the alpha-cubic phase of FAPbI₃, and rutile tetragonal SnO₂. Following the optimization of SnO₂ (cell size: 16.7, 16.7, 11.58 Å) using a Monkhorst–Pack k-point grid of $5 \times 5 \times 7$, a slab of MAPbBr₃ and FAPbI₃ was positioned on the SnO₂ surface with a 20 Å vacuum along the vertical axis to remove the interactions between neighboring layers in the interface direction. Full optimization was then used to obtain models for SnO₂-FAPbI₃ and SnO₂-MAPbBr₃. A third model consisted of both MAPbBr3 and FAPbI3 on SnO2 laterally stacked, with MAPbBr3 being a minority component. From these three models, RDFs for all atoms were computed to help understand how the ions distribute. The RDFs for the heterostructures with MAPbBr₃ and FAPbI3 did not show marked changes in the cation-anion distribution. This suggests that the lowest strain should provide the best performance.

ASSOCIATED CONTENT

Supporting Information

The Supporting Information is available free of charge at https://pubs.acs.org/doi/10.1021/acsami.3c03520.

A detailed list of perovskite and SnO_2 grain size and mean square roughness calculations, $J{-}V$ curves of perovskites and corresponding table of parameters, $I{-}V$ curves of bare SnO_2 films, $W{-}H$ plot analysis plots and corresponding tables of crystallite size and micro-strain for perovskite and SnO_2 , XRD of perovskite, RDF calculations of $MAPbI_3$ and $FAPbI_3$, NMF plots highlighting interfacial regions for all perovskite films, mass spectra gathered from ToF-SIMS in positive and negative ion modes, ToF-SIMS negative ion mode measurements, additional depth profiles of all ions, and c-AFM of light-soaked perovskite films (PDF)

AUTHOR INFORMATION

Corresponding Authors

Mahshid Ahmadi — Department of Materials Science and Engineering, Institute for Advanced Materials and Manufacturing, University of Tennessee, Knoxville, Tennessee 37920, United States; Occid.org/0000-0002-3268-7957; Email: mahmadi3@utk.edu

Olga S. Ovchinnikova — Department of Materials Science and Engineering, Institute for Advanced Materials and Manufacturing, University of Tennessee, Knoxville, Tennessee 37920, United States; Occid.org/0000-0001-8935-2309; Email: oovchinn@vols.utk.edu

Authors

Holland Hysmith — Bredesen Center for Interdisciplinary Research, University of Tennessee, Knoxville, Tennessee 37996, United States; © orcid.org/0000-0003-0222-6743

So Yeon Park – National Renewable Energy Laboratory, Golden, Colorado 80401, United States; orcid.org/0000-0001-6774-0941

Jonghee Yang — Department of Materials Science and Engineering, Institute for Advanced Materials and Manufacturing, University of Tennessee, Knoxville, Tennessee 37920, United States; orcid.org/0000-0001-7013-6761

Anton V. Ievlev — Center for Nanophase Materials Sciences, Oak Ridge National Laboratory, Oak Ridge, Tennessee 37830, United States; orcid.org/0000-0003-3645-0508

Yongtao Liu — Center for Nanophase Materials Sciences, Oak Ridge National Laboratory, Oak Ridge, Tennessee 37830, United States; orcid.org/0000-0003-0152-1783

Kai Zhu — National Renewable Energy Laboratory, Golden, Colorado 80401, United States; orcid.org/0000-0003-0908-3909

Bobby G. Sumpter — Center for Nanophase Materials Sciences, Oak Ridge National Laboratory, Oak Ridge, Tennessee 37830, United States; orcid.org/0000-0001-6341-0355

Joseph Berry — National Renewable Energy Laboratory, Golden, Colorado 80401, United States

Complete contact information is available at: https://pubs.acs.org/10.1021/acsami.3c03520

Author Contributions

H.H.: wrote the manuscript, performed ToF-SIMS and c-AFM measurements, calculated NMF and W-H plot analysis.

S.Y.P.: synthesized the samples, performed XRD measurements, calculated W—H plot analysis. J.Y.: revised the manuscript, provided feedback on experiments. A.I.: helped with ToF-SIMS measurements and NMF calculations. Y.T.: revised the manuscript, provided feedback on experiments. K.Z.: provided feedback on experiments. B.S.: calculated RDFs. J.B.: revised the manuscript, provided feedback on experiments. M.A.: directed experiments, revised the manuscript. O.O.: directed experiments, revised the manuscript.

Notes

The authors declare no competing financial interest.

ACKNOWLEDGMENTS

This research was funded by the DOE Office of Science Research Program for Microelectronics Codesign (sponsored by ASCR, BES, HEP, NP, and FES) through the Abisko Project with program managers Robinson Pino (ASCR). Hal Finkel (ASCR), and Andrew Schwartz (BES) and was performed at the Center for Nanophase Materials Sciences (CNMS), a U.S. Department of Energy, Office of Science User Facility. M.A. was supported from the National Science Foundation (NSF), Award Number No. 2043205. ToF-SIMS characterization was conducted at the Center for Nanophase Materials Sciences, which is a DOE Office of Science User Facility, and using instrumentation within ORNL's Materials Characterization Core provided by UT-Battelle, LLC under Contract No. DE-AC05-00OR22725 with the U.S. Department of Energy.

REFERENCES

- (1) Min, H.; Lee, D. Y.; Kim, J.; Kim, G.; Lee, K. S.; Kim, J.; Paik, M. J.; Kim, Y. K.; Kim, K. S.; Kim, M. G.; et al. Perovskite solar cells with atomically coherent interlayers on SnO2 electrodes. *Nature* **2021**, 598, 444–450.
- (2) Wang, B.; Novendra, N.; Navrotsky, A. Energetics, Structures, and Phase Transitions of Cubic and Orthorhombic Cesium Lead Iodide (CsPbI3) Polymorphs. *J. Am. Chem. Soc.* **2019**, *141*, 14501–14504.
- (3) Tsai, H.; Asadpour, R.; Blancon, J.-C.; Stoumpos, C. C.; Durand, O.; Strzalka, J. W.; Chen, B.; Verduzco, R.; Ajayan, P. M.; Tretiak, S.; et al. Light-induced lattice expansion leads to high-efficiency perovskite solar cells. *Science* **2018**, *360*, *67*–70.
- (4) Wang, Y.; Zhang, T.; Kan, M.; Li, Y.; Wang, T.; Zhao, Y. Efficient α -CsPbI3 Photovoltaics with Surface Terminated Organic Cations. *Joule* **2018**, 2, 2065–2075.
- (5) Tiep, N. H.; Ku, Z.; Fan, H. J. Recent Advances in Improving the Stability of Perovskite Solar Cells. *Adv. Energy Mater.* **2016**, *6*, 1501420.
- (6) Kim, J.; Lee, S.-H.; Lee, J. H.; Hong, K.-H. The Role of Intrinsic Defects in Methylammonium Lead Iodide Perovskite. *J. Phys. Chem. Lett.* **2014**, *5*, 1312–1317.
- (7) Dunfield, S. P.; Bliss, L.; Zhang, F.; Luther, J. M.; Zhu, K.; Hest, M. F. A. M.; Reese, M. O.; Berry, J. J. From Defects to Degradation: A Mechanistic Understanding of Degradation in Perovskite Solar Cell Devices and Modules. *Adv. Energy Mater.* **2020**, *10*, 1904054.
- (8) Chen, S.; Dai, X.; Xu, S.; Jiao, H.; Zhao, L.; Huang, J. Stabilizing perovskite-substrate interfaces for high-performance perovskite modules. *Science* **2021**, *373*, 902–907.
- (9) Abdelsamie, M.; Xu, J.; Bruening, K.; Tassone, C. J.; Steinrück, H.-G.; Toney, M. F. Impact of Processing on Structural and Compositional Evolution in Mixed Metal Halide Perovskites during Film Formation. *Adv. Funct. Mater.* **2020**, *30*, 2001752.
- (10) Wang, F.; Bai, S.; Tress, W.; Hagfeldt, A.; Gao, F. Defects engineering for high-performance perovskite solar cells. *npj Flexible Electron.* **2018**, *2*, 22.

- (11) Brenes, R.; Guo, D.; Osherov, A.; Noel, N. K.; Eames, C.; Hutter, E. M.; Pathak, S. K.; Niroui, F.; Friend, R. H.; Islam, M. S.; et al. Metal Halide Perovskite Polycrystalline Films Exhibiting Properties of Single Crystals. *Joule* **2017**, *1*, 155–167.
- (12) Ou, Q.-D.; Li, C.; Wang, Q.-K.; Li, Y.-Q.; Tang, J.-X. Recent Advances in Energetics of Metal Halide Perovskite Interfaces. *Adv. Mater. Interfaces* **2017**, *4*, 1600694.
- (13) DuBose, J. T.; Kamat, P. V. TiO2-Assisted Halide Ion Segregation in Mixed Halide Perovskite Films. *J. Am. Chem. Soc.* **2020**, 142, 5362–5370.
- (14) Park, H.; Chaurasiya, R.; Jeong, B. H.; Sakthivel, P.; Park, H. J. Nickel Oxide for Perovskite Photovoltaic Cells. *Adv. Photonics Res.* **2021**, 2, 2000178.
- (15) Han, G. S.; Song, Y. H.; Jin, Y. U.; Lee, J.-W.; Park, N.-G.; Kang, B. K.; Lee, J.-K.; Cho, I. S.; Yoon, D. H.; Jung, H. S. Reduced Graphene Oxide/Mesoporous TiO₂ Nanocomposite Based Perovskite Solar Cells. *ACS Appl. Mater. Interfaces* **2015**, *7*, 23521–23526.
- (16) Gao, X.-X.; Ge, Q.-Q.; Xue, D.-J.; Ding, J.; Ma, J.-Y.; Chen, Y.-X.; Zhang, B.; Feng, Y.; Wan, L.-J.; Hu, J.-S. Tuning the Fermi-level of TiO₂ mesoporous layer by lanthanum doping towards efficient perovskite solar cells. *Nanoscale* **2016**, *8*, 16881–16885.
- (17) Zhang, H.; Cheng, J.; Lin, F.; He, H.; Mao, J.; Wong, K. S.; Jen, A. K. Y.; Choy, W. C. H. Pinhole-Free and Surface-Nanostructured NiOx Film by Room-Temperature Solution Process for High-Performance Flexible Perovskite Solar Cells with Good Stability and Reproducibility. *ACS Nano* **2016**, *10*, 1503—1511.
- (18) Azpiroz, J. M.; Mosconi, E.; Bisquert, J.; De Angelis, F. Defect migration in methylammonium lead iodide and its role in perovskite solar cell operation. *Energy Environ. Sci.* **2015**, *8*, 2118–2127.
- (19) Altinkaya, C.; Aydin, E.; Ugur, E.; Isikgor, F. H.; Subbiah, A. S.; De Bastiani, M.; Liu, J.; Babayigit, A.; Allen, T. G.; Laquai, F.; et al. Tin Oxide Electron-Selective Layers for Efficient, Stable, and Scalable Perovskite Solar Cells. *Adv. Mater.* **2021**, *33*, 2005504.
- (20) Hao, M.; Duan, T.; Ma, Z.; Ju, M.-G.; Bennett, J. A.; Liu, T.; Guo, P.; Zhou, Y. Flattening Grain-Boundary Grooves for Perovskite Solar Cells with High Optomechanical Reliability. *Adv. Mater.* **2023**, 35, No. e2211155.
- (21) Xiong, L.; Guo, Y.; Wen, J.; Liu, H.; Yang, G.; Qin, P.; Fang, G. Review on the Application of SnO_2 in Perovskite Solar Cells. *Adv. Funct. Mater.* **2018**, 28, 1802757.
- (22) Kim, S.; Yun, Y. J.; Kim, T.; Lee, C.; Ko, Y.; Jun, Y. Hydrolysis-Regulated Chemical Bath Deposition of Tin-Oxide-Based Electron Transport Layers for Efficient Perovskite Solar Cells with a Reduced Potential Loss. *Chem. Mater.* **2021**, *33*, 8194–8204.
- (23) Yi, H.; Wang, D.; Mahmud, M. A.; Haque, F.; Upama, M. B.; Xu, C.; Duan, L.; Uddin, A. Bilayer SnO₂ as Electron Transport Layer for Highly Efficient Perovskite Solar Cells. *ACS Appl. Energy Mater.* **2018**, *1*, 6027–6039.
- (24) Yoo, J. J.; Seo, G.; Chua, M. R.; Park, T. G.; Lu, Y.; Rotermund, F.; Kim, Y.-K.; Moon, C. S.; Jeon, N. J.; Correa-Baena, J.-P.; et al. Efficient perovskite solar cells via improved carrier management. *Nature* **2021**, *590*, 587–593.
- (25) Wang, P.; Wang, J.; Zhang, X.; Wang, H.; Cui, X.; Yuan, S.; Lu, H.; Tu, L.; Zhan, Y.; Zheng, L. Boosting the performance of perovskite solar cells through a novel active passivation method. *J. Mater. Chem. A* **2018**, *6*, 15853–15858.
- (26) Maniammal, K.; Madhu, G.; Biju, V. X-ray diffraction line profile analysis of nanostructured nickel oxide: Shape factor and convolution of crystallite size and microstrain contributions. *Phys. E (Amsterdam, Neth.)* **2017**, 85, 214–222.
- (27) Shafi, P. Impact of crystalline defects and size on X-ray line broadening: A phenomenological approach for tetragonal SnO2 nanocrystals. *AIP Adv.* **2015**, *5*, No. 057137.
- (28) Chen, B.; Li, T.; Dong, Q.; Mosconi, E.; Song, J.; Chen, Z.; Deng, Y.; Liu, Y.; Ducharme, S.; Gruverman, A.; et al. Large electrostrictive response in lead halide perovskites. *Nat. Mater.* **2018**, 17, 1020–1026.
- (29) Oka, D.; Hirose, Y.; Matsui, F.; Kamisaka, H.; Oguchi, T.; Maejima, N.; Nishikawa, H.; Muro, T.; Hayashi, K.; Hasegawa, T.

- Strain Engineering for Anion Arrangement in Perovskite Oxynitrides. *ACS Nano* **2017**, *11*, 3860–3866.
- (30) Travis, W.; Glover, E. N. K.; Bronstein, H.; Scanlon, D. O.; Palgrave, R. G. On the application of the tolerance factor to inorganic and hybrid halide perovskites: a revised system. *Chem. Sci.* **2016**, *7*, 4548–4556.
- (31) Harvey, S. P.; Messinger, J.; Zhu, K.; Luther, J. M.; Berry, J. J. Investigating the Effects of Chemical Gradients on Performance and Reliability within Perovskite Solar Cells with TOF-SIMS. *Adv. Energy Mater.* **2020**, *10*, 1903674.
- (32) Noël, C.; Busby, Y.; Mine, N.; Houssiau, L. ToF-SIMS Depth Profiling of Organic Delta Layers with Low-Energy Cesium Ions: Depth Resolution Assessment. *J. Am. Soc. Mass Spectrom.* **2019**, *30*, 1537–1544.
- (33) Higgins, K.; Lorenz, M.; Ziatdinov, M.; Vasudevan, R. K.; Ievlev, A. V.; Lukosi, E. D.; Ovchinnikova, O. S.; Kalinin, S. V.; Ahmadi, M. Exploration of Electrochemical Reactions at Organic—Inorganic Halide Perovskite Interfaces via Machine Learning in In Situ Time-of-Flight Secondary Ion Mass Spectrometry. *Adv. Funct. Mater.* **2020**, *30*, 2001995.
- (34) Kim, D.; Liu, Y.; Ievlev, A. V.; Higgins, K.; Ovchinnikova, O. S.; Yun, J. S.; Seidel, J.; Kalinin, S. V.; Ahmadi, M. Unraveling the hysteretic behavior at double cations-double halides perovskite electrode interfaces. *Nano Energy* **2021**, *89*, No. 106428.
- (35) Bi, C.; Zheng, X.; Chen, B.; Wei, H.; Huang, J. Spontaneous Passivation of Hybrid Perovskite by Sodium Ions from Glass Substrates: Mysterious Enhancement of Device Efficiency Revealed. *ACS Energy Lett.* **2017**, *2*, 1400–1406.
- (36) Bang, S.-M.; Shin, S. S.; Jeon, N. J.; Kim, Y. Y.; Kim, G.; Yang, T.-Y.; Seo, J. Defect-Tolerant Sodium-Based Dopant in Charge Transport Layers for Highly Efficient and Stable Perovskite Solar Cells. *ACS Energy Lett.* **2020**, *5*, 1198–1205.
- (37) Douhéret, O.; Lutsen, L.; Swinnen, A.; Breselge, M.; Vandewal, K.; Goris, L.; Manca, J. Nanoscale electrical characterization of organic photovoltaic blends by conductive atomic force microscopy. *Appl. Phys. Lett.* **2006**, 89, No. 032107.
- (38) Yang, J.; LaFollette, D. K.; Lawrie, B. J.; Ievlev, A. V.; Liu, Y.; Kelley, K. P.; Kalinin, S. V.; Correa-Baena, J.-P.; Ahmadi, M. Understanding the Role of Cesium on Chemical Complexity in Methylammonium-Free Metal Halide Perovskites. *Adv. Energy Mater.* **2022**, *n/a*, 2202880.
- (39) Castro-Méndez, A.-F.; Hidalgo, J.; Correa-Baena, J.-P. The Role of Grain Boundaries in Perovskite Solar Cells. *Adv. Energy Mater.* **2019**, *9*, 1901489.
- (40) Song, J.; Zhou, Y.; Padture, N. P.; Huey, B. D. Anomalous 3D nanoscale photoconduction in hybrid perovskite semiconductors revealed by tomographic atomic force microscopy. *Nat. Commun.* **2020**, *11*, 3308.
- (41) Leblebici, S. Y.; Leppert, L.; Li, Y.; Reyes-Lillo, S. E.; Wickenburg, S.; Wong, E.; Lee, J.; Melli, M.; Ziegler, D.; Angell, D. K.; et al. Facet-dependent photovoltaic efficiency variations in single grains of hybrid halide perovskite. *Nat. Energy* **2016**, *1*, 16093.
- (42) Si, H.; Zhang, S.; Ma, S.; Xiong, Z.; Kausar, A.; Liao, Q.; Zhang, Z.; Sattar, A.; Kang, Z.; Zhang, Y. Emerging conductive atomic force microscopy for metal halide perovskite materials and solar cells. *Adv. Energy Mater.* **2020**, *10*, 1903922.
- (43) Zhou, Y.; Herz, L. M.; Jen, A. K. Y.; Saliba, M. Advances and challenges in understanding the microscopic structure–property–performance relationship in perovskite solar cells. *Nat. Energy* **2022**, *7*, 794–807.
- (44) Liu, Y.; Yang, J.; Lawrie, B. J.; Kelley, K. P.; Ziatdinov, M.; Kalinin, S. V.; Ahmadi, M. Disentangling Electronic Transport and Hysteresis at Individual Grain Boundaries in Hybrid Perovskites via Automated Scanning Probe Microscopy. *ACS Nano* **2023**, 9647.
- (45) Yang, J.; Lee, J.; Lee, J.; Yi, W. Oxygen annealing of the ZnO nanoparticle layer for the high-performance PbS colloidal quantum-dot photovoltaics. *J. Power Sources* **2019**, *421*, 124–131.
- (46) Park, S. Y.; Shim, H.C. Highly Efficient and Air-Stable Heterostructured Perovskite Quantum Dot Solar Cells Using a Solid-

- State Cation-Exchange Reaction. ACS Appl. Mater. Interfaces 2020, 12 (51), 57124-57133.
- (47) Zhang, F.; Park, S. Y.; Yao, C.; Lu, H.; Dunfield, S. P.; Xiao, C.; Uličná, S.; Zhao, X.; Du Hill, L.; Chen, X.; et al. Metastable Dion-Jacobson 2D structure enables efficient and stable perovskite solar cells. *Science* **2022**, *375*, 71–76.
- (48) Fabian Pedregosa, G. V.; Gramfort, A.; Michel, V.; Thirion, B.; Grisel, O.; Blondel, M.; Prettenhofer, P.; Weiss, R.; Dubourg, V.; Vanderplas, J.; Passos, A.; Cournapeau, D.; Brucher, M.; Perrot, M.; Duchesnay, É. Scikit-learn: Machine learning in Python. *J. Mach. Learn. Technol.* **2011**, *12*, 2825–2830.
- (49) Kresse, G.; Furthmüller, J. Efficient iterative schemes for ab initio total-energy calculations using a plane-wave basis set. *Phys. Rev. B* **1996**, *54*, 11169–11186.
- (50) Vanderbilt, D. Soft self-consistent pseudopotentials in a generalized eigenvalue formalism. *Phys. Rev. B* **1990**, *41*, 7892–7895.
- (51) Klimeš, J.; Bowler, D. R.; Michaelides, A. Van Der Waals density functionals applied to solids. *Phys. Rev. B* **2011**, 83, No. 195131.
- (52) Zhang, L.; Sit, P. H. L. *Ab Initio* Study of Interaction of Water, Hydroxyl Radicals, and Hydroxide Ions with CH₃NH₃PbI₃ and CH₃NH₃PbBr₃ Surfaces. *J. Phys. Chem. C* **2015**, *119*, 22370–22378.
- (53) Weller, M. T.; Weber, O. J.; Frost, J. M.; Walsh, A. Cubic Perovskite Structure of Black Formamidinium Lead Iodide, α-[HC(NH2)2]PbI3, at 298 K. J. Phys. Chem. Lett. **2015**, 6, 3209–3212